Solar RRL

WILEY VCH

Solar RRL

RESEARCH ARTICLE OPEN ACCESS

Optical Reabsorption Effects in Photoluminescence of Perovskites Conformally Coated on Textured Silicon

Adrian Callies[1] | Oussama Er-Raji[1] | Robin Schot[2] | Stefan Lange[3] | Benedikt Bläsi[1] | Tom Veeken[2] | Karsten Buse[4,5] | Albert Polman[2] | Stefan W. Glunz[1,6] | Juliane Borchert[1,6] | Oliver Höhn[1,6] | Patricia S. C. Schulze[1]

[1]Fraunhofer Institute for Solar Energy Systems, ISE, Freiburg, Germany | [2]NWO-Institute AMOLF, Amsterdam, Netherlands | [3]Fraunhofer Center for Silicon Photovoltaics CSP, Halle, Germany | [4]Fraunhofer Institute for Physical Measurement Techniques IPM, Freiburg, Germany | [5]Laboratory for Optical Systems, Department of Microsystems Engineering - IMTEK, University of Freiburg, Freiburg, Germany | [6]Chair of Photovoltaic Energy Conversion, Department of Sustainable Systems Engineering (INATECH), University of Freiburg, Freiburg, Germany

Correspondence: Adrian Callies (adrian.callies@ise.fraunhofer.de) | Oussama Er-Raji (oussama.er-raji@ise.fraunhofer.de)

Received: 20 January 2025 | **Revised:** 10 March 2025 | **Accepted:** 12 March 2025

Funding: Fraunhofer Gesellschaft, Grant/Award Numbers: MEEt MaNiTU; German Federal Ministry for Economic Affairs and Climate Action, Grant/Award Number: 03EE1086A; ERC, Grant/Award Number: 101125948; Vector Stiftung's funding of J. Borchert's Independent Research Group; Deutsche Bundesstiftung Umwelt, Grant/Award Number: 20021/728-242; Netherlands National Growth Fund, Grant/Award Number: SolarNL

Keywords: bandgap | perovskite silicon tandem solar cells | photoluminescence | photovoltaic | random pyramids

ABSTRACT

Two-terminal fully textured perovskite silicon tandem solar cells have recently advanced significantly and are quickly moving toward scalable production. While µm-sized texturing of the silicon solar cell enables minimizing reflection losses, and tuning of the perovskite layer thickness allows optimizing the photo-generated current distribution between subcells, both approaches introduce challenges at the development stage. One of these challenges is the accurate optoelectronic assessment of perovskite films with photoluminescence (PL) spectroscopy. In this work, we study effects of optical self-absorption on the PL of perovskite films conformally coated on industry-compatible textured silicon with pyramid heights ranging from <1 to >6 µm. Our findings indicate that with increasing pyramid height, the PL peak energy shows a redshift of 20–30 meV. Similarly, increasing the perovskite thickness on a fixed texture pattern induces a redshift. Three-dimensional confocal laser scanning PL microscopy, combined with statistical ray optical simulations, reveals that photon reabsorption in the perovskite film plays an important role in the texture-dependent and thickness-dependent PL responses. This optical effect, besides previously reported changes in perovskite mechanical properties due to silicon texture, is crucial to consider for accurate assessment of PL, and for efficient optimization of perovskite silicon tandems with advanced optical designs.

1 | Introduction

Perovskite–silicon tandem solar cells present one of the most prominent emerging solar cell technologies of the last decade. They have seen rapid progress in recent years, outperforming the conversion efficiency of single-junction silicon devices at cell and module level. Given the strong industrialization potential of this technology, it is crucial to adopt industry-compatible processes and solar cell architectures. For two-terminal devices, the fully textured tandem solar cell architecture stands out for its use of industry-compatible textured silicon (pyramid height >1 µm) and its superior light scattering scheme [1–4]. In the perovskite top-cell, the perovskite absorber is typically deposited via the hybrid evaporation/spin coating route enabling a conformal formation on such large silicon pyramids [5]. As we have recently demonstrated, this method enables the fabrication

Adrian Callies and Oussama Er-Raji contributed equally to this study.

of high-efficiency devices with a power conversion efficiency exceeding 30% [6–8]. Conformally coated textured geometries can also be realized by blade- and slot-die coating, allowing for scalability to industrial-scale processing [9–12].

To further enhance device performance and process reproducibility, it is crucial to understand the influence of the silicon surface texture on the perovskite layer and to identify potential effects of inhomogeneities in the coated pyramid geometry. Photoluminescence (PL) spectroscopy is a common technique to probe the bandgap and charge carrier lifetime of the perovskite layer. In this method, a light source (sunlight, LED, laser) is used to create free charge carriers in the absorber and the resulting radiation due to radiative recombination is probed. It is often used for characterization, in-line process control, and outdoor monitoring [13–18]. Research on perovskite films deposited on planar substrates showed a consistent redshifting of the PL emission with increasing layer thickness, suggesting an effect of reabsorption [19–21]. In characterization of the bandgap of silicon wafers, this reabsorption effect was utilized to obtain depth-resolved information [22].

PL measurements on textured geometries are more complex to analyze due to the complex outcoupling of light in the textured topology, where light is reflected and refracted at multiple interfaces before it couples out. Earlier work showed that when measuring PL of similarly fabricated perovskite absorbers on substrates with a varying texture, a variation in PL peak energy is observed [23–25]. Reabsorption effects have been identified as an at least correlating factor [24], but to our knowledge no quantification of the optical effect, proving causality, has been provided so far. Inhomogeneities in mechanical strain or stress have been suggested as an additional explanation for the perovskite PL redshift in the case of textured substrates [23, 25]. These earlier data raise the question of how significant the effects of optical reabsorption in textured geometries are and how they also compare to the reabsorption effects caused by varying film thickness. The latter comparison is especially important when a texture change correlates with a reduction or increase of the perovskite layer thickness due to the nature of the deposition method. Given the high potential of conformally coated textured tandem devices detailed understanding of these effects is essential to interpret optical spectra that are taken to characterize the materials bandgap and the effect of materials inhomogeneities.

Here, we present a systematic analysis of the PL spectra for similarly fabricated perovskite absorbers based on a methylammonium-free double-cation double-halide composition with varying thicknesses on both planar and random pyramid-textured substrates. Different pyramid heights ranging from <1 to >6 μm were included in the study, and PL was measured with a macroscopic focus (0.1 cm^2 spot-size) on the sample surface and in 3D using confocal scanning PL microscopy. To interpret the data regarding reabsorption, we present a statistical ray-optics model that takes into account reflection and refraction at all interfaces in the perovskite texture as well as absorption using measured optical constants. By combining measurements and simulations we conclude that optical reabsorption leads to significant redshifts and explains the majority of the experimentally observed redshift in the textured structures.

2 | Results and Discussion

2.1 | Effect of Perovskite Layer Thickness

We prepared samples with three different perovskite layer thicknesses on planar and textured substrates. Perovskite fabrication was done using the hybrid evaporation/spin coating route which enables a conformal layer formation on both substrate types. The fabrication method consists of reacting thermally evaporated perovskite precursors (PbI_2 and CsI) with subsequent wet-chemically deposited organic precursors (FABr and FAI, FA denotes formamidinium) during an annealing step (more details in the Experimental Section) [26]. It results in the formation of photostable double-cation double-halide perovskite thin films and was previously implemented to obtain high-efficiency devices [6–8, 27, 28].

To obtain different perovskite thicknesses, we evaporated three distinct thicknesses of the inorganic scaffold, namely, 250, 400, and 550 nm. We note that due to the texture factor, a thinner scaffold thickness is obtained on textured silicon substrates compared to planar silicon substrates as detailed in Figure S1a. Then, the concentration of the organic precursors was optimized for each substrate and each scaffold thickness to allow full conversion of precursors to the perovskite absorber with minimal excess/residual precursors phases, as summarized in Section S1. For thick layers, a limited conversion could be noted due to the organohalide diffusion limitation, but this does not impact the PL peak position as demonstrated in our earlier work [28].

Figure 1a shows cross-sectional scanning electron microscopy (SEM) images of the perovskite absorbers deposited on planar and textured substrates. Three distinct perovskite thicknesses were obtained on each substrate type as summarized in Figure S1c,d (450, 800, and 1000 nm on planar silicon, and 300, 500, and 650 nm on textured silicon, measured normal to the silicon pyramid surface). This allows a direct investigation of the effect of perovskite layer thickness on the PL response.

Figure 1b shows the measured change in PL peak energy when the substrate type and perovskite thickness are varied, and Figure S3a,b presents representative spectrally-resolved PL spectra. With increasing perovskite thickness, the peak shifts to lower energies (redshift) on both planar and textured substrates. Within the respective thickness regions investigated, a linear fit can be utilized to obtain the local slope of this change: For the textured silicon surface it is −47 meV/μm in the thickness range 300–650 nm, while for the planar substrate, it is −27 meV/μm in the 450–1000 nm thickness range. We note that with a significantly larger thickness range, the PL peak energy is expected to converge toward a limit value based on the exponential nature of the absorption process.

To determine how much of this thickness dependence can be ascribed to reabsorption in the perovskite film, optical simulations were performed using a ray-tracing model, as described in the Experimental Section. The optical constants for the simulations were determined experimentally, as described in the Experimental Section as well. We note that to represent a PL experiment, also the 3D distribution of the carrier generation rate must be taken into account. We have assumed that, while the 3D

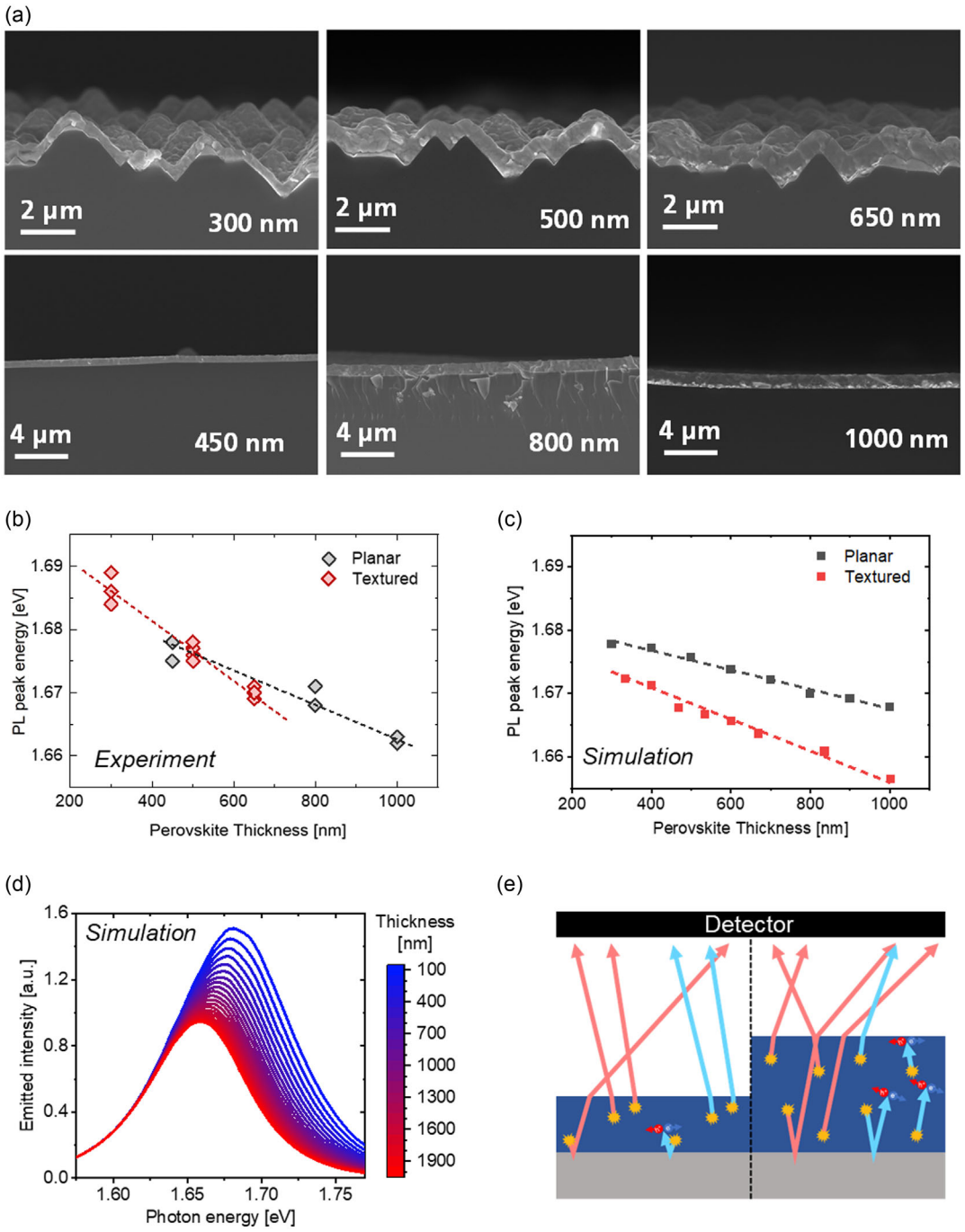

FIGURE 1 | (a) Cross-sectional electron microscopy (SEM) images of perovskite thin films with three different thicknesses on planar and textured silicon substrates. The average perovskite thickness is noted on the bottom right side of the images (for thickness distribution see Figure S1c,d). (b) PL peak energies for perovskite layers with different thicknesses on planar and ~3 µm random pyramid textured substrates. For each thickness/texture combination, two substrates were fabricated. Multiple measurements per sample and measurements for both samples are included if available. (c) Simulated PL peak energy for different perovskite thicknesses on a planar and a 3 µm pyramid substrate. (d) Simulated PL spectrum for different perovskite thicknesses on a planar sample. (e) Illustration of the reabsorption process. With thicker perovskite, absorption increases, in particular of high-energy photons. This results in a redshift of the measured PL spectrum.

pump absorption profile in the texture is complex, the generation profile is constant throughout the perovskite layer because of carrier diffusion. The homogeneous excitation distribution is then represented in the statistical model by a collection of randomly placed light-emitting point sources throughout the perovskite film. Details on these assumptions can also be found in the Experimental Section.

Figure 1d shows the simulated spectra for planar films with a thickness ranging from 100 to 2000 nm. For all thicknesses, the depth-integrated generation rate within the sample is taken identical. It is observed that with increasing thickness, the spectrum progressively redshifts as a result of increased reabsorption, reproducing the effect observed in experiment. Figure 1e illustrates the reabsorption effect: at larger thicknesses, reabsorption

TABLE 1 | Local slopes for the rate of change of the PL peak energy.

	Local rate of change [meV/μm]	
Substrate	**Experiment**	**Simulation**
Textured (300–650 nm)	−47	−25
Planar (450–1000 nm)	−27	−15

is more pronounced. As higher-energy photons are more prone to reabsorption, this results in a redshift of the emitted signal. Figure 1c shows the simulated PL peak energy for perovskite thicknesses in the range 300–1000 nm for the planar and textured films. As with the experimental data, a local slope of the PL peak energy change rate for this range can be obtained using a linear fit: for the planar sample, the simulated PL peak energy shifts by −15 meV/μm, while for the textured sample, the local slope equals −25 meV/μm. By comparing the measured and simulated redshifts in Table 1 for increasing thickness, we conclude that optical reabsorption contributes a major fraction to the spectral shift in the PL spectrum. Differences between the simulation and experiment regarding the rate of change in PL peak position may be attributed to scattering at grain boundaries, which was not included in the simulation model, as currently, no quantitative description of this effect exists. Qualitatively, the absorption and scattering at these boundaries lead to a longer optical path length within the perovskite material before the air–perovskite interface is reached. This enhances reabsorption, thereby increasing the redshift effect for a given perovskite layer thickness variation as well as for a texture change.

2.2 | Effect of Silicon Surface Texture Height

Aforementioned, the effect of using a textured opposed to a planar perovskite–silicon interface has already been shown. In the next part, the impact of the pyramid size is further examined. For this, a perovskite absorber with constant thickness of 650 ± 50 nm was deposited on a series of silicon substrates with average pyramid heights between 1 μm and more than 6 μm (Figure 2a). The measured PL peak energy (measurement with spot size of 0.1 cm^2) of these samples is displayed in Figure 2b, and S3c presents representative spectrally resolved PL spectra. It can be observed that with increasing pyramid height, a blue-shift of the PL signal occurs. From the smallest to largest pyramid size, the peak energy shifts by more than 10 meV toward higher energy values. Scattering in the data is attributed to variation in the pyramid geometry and perovskite thickness.

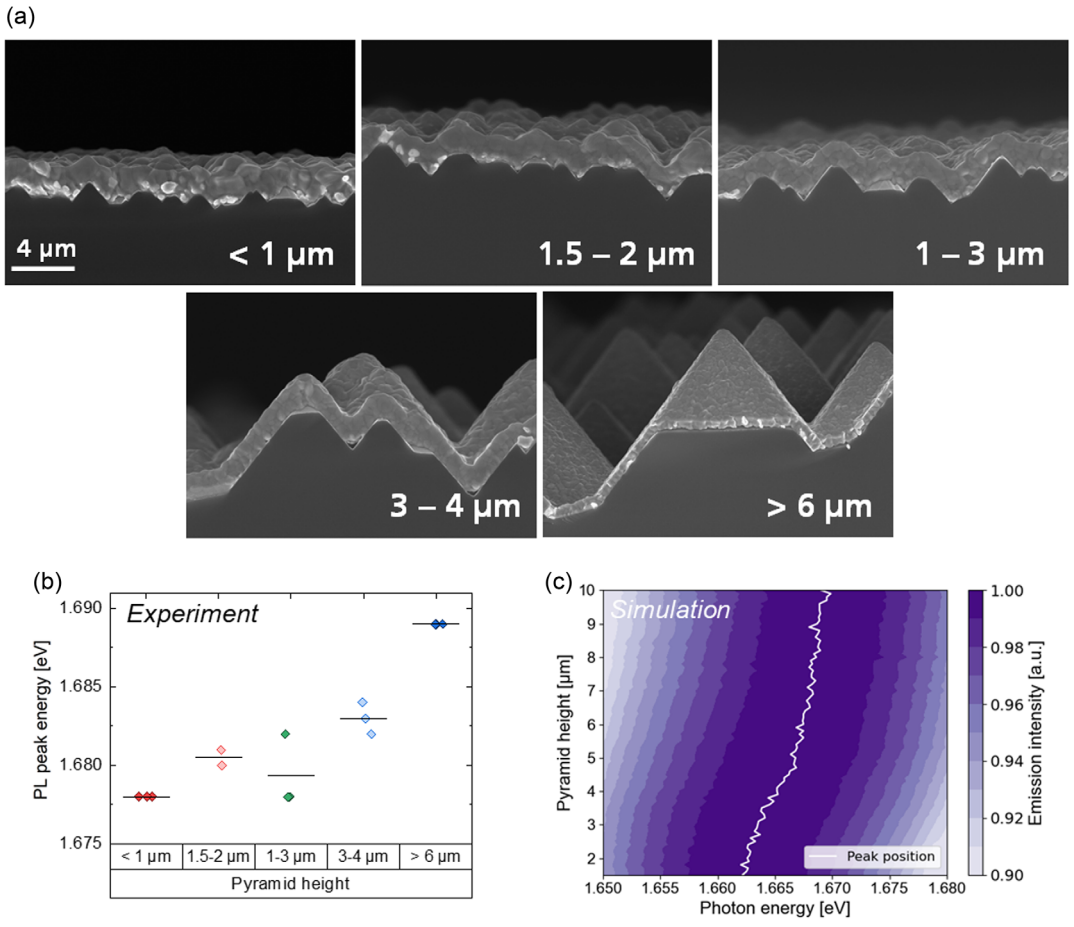

FIGURE 2 | Influence of silicon pyramid height on perovskite PL emission. (a) SEM images of the perovskite absorbers deposited on silicon substrates with different pyramid heights ranging systematically from <1 to >6 μm. (b) Experimental PL peak energy for different pyramid heights for a perovskite layer thickness normal to the pyramid surface of 650 ± 50 nm. (c) Simulated PL spectrum (intensity displayed by color intensity) for different pyramid heights. The peak energies are marked with the white line. In the simulation, a perovskite thickness normal to the pyramid surface of 670 nm is used.

To study the origin of the optical effects causing the peak shift with changing pyramid height, PL spectra were simulated for varying pyramid heights using the raytracing model. A constant perovskite thickness of 670 nm normal to the pyramid surface was utilized and the pyramid height was varied from 1.5 to 10 μm. Figure 2c shows the resulting PL spectra, which show a peak energy increase by around 5 meV across the range of heights simulated. In addition, the simulation results systematically show lower peak energies than the experiments, in line with what was observed for the textured samples in Figure 1c. The underlying optical effects are discussed in the next section. Furthermore, PL peak shifts ascribed to perovskite compositional changes due to varying pyramid sizes were assessed and found to be minimal, as described in detail in Section S3.

2.3 | 3D-Resolved PL Emission

To explore the origin of the texture-dependent shift of the PL peak energy, we conducted 3D spatially resolved PL measurements using confocal scanning optical microscopy. A WITec alpha300 RS confocal microscopy setup in reflection mode was used, with a 100x objective and a numerical aperture of 0.9. The textured samples were excited with a 405 nm excitation wavelength continuous-wave laser with 5 μW power, and a spot size with a $1/e^2$ diameter of approximately 500 nm. 2D PL maps of 40×40 μm were taken by moving the sample with a piezoelectrically activated stage for subsequent height steps of 500 nm between each successive map. We note that under some irradiation conditions halide segregation can take place in perovskite layers leading to an artificial PL redshift. The effect of this redshift on the resulting measurement was mitigated by appropriate choice of illumination intensity and scan direction as described in the Experimental Section.

To analyze the 3D confocal data set, we determined for each x–y position the confocal excitation/collection height at which the maximum PL intensity is observed. Figure 3a shows the distribution of PL peak energy at that height for a texture with random pyramids with an average height of 3–4 μm. Distinct regions with the PL signal shifted toward higher (blue in Figure 3a) and lower (red in Figure 3a) energies can be observed. As visible in the camera image of the same area of the sample in Figure 3b, these regions are correlated to the peaks and valleys of the random pyramid texture, respectively.

To understand how reabsorption contributes to the PL peak energy shift observed in experiment, localized emission is

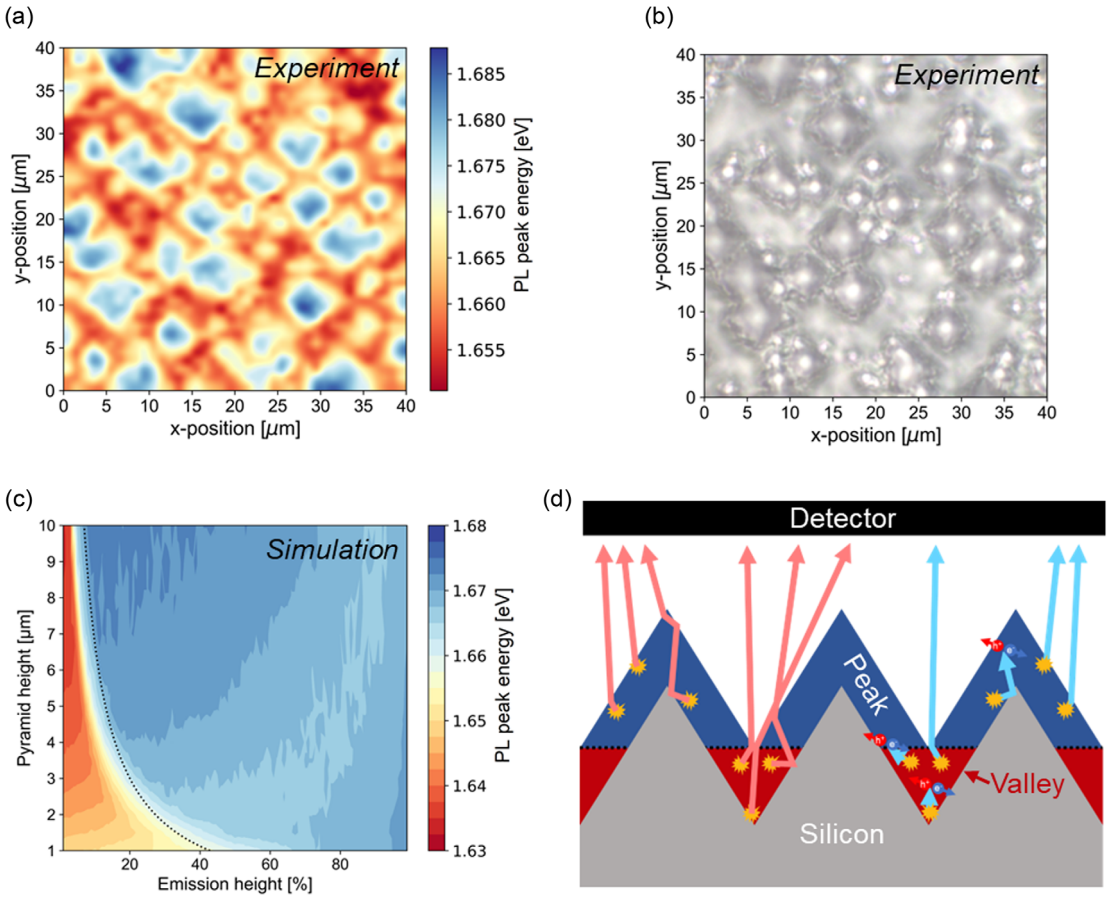

FIGURE 3 | Influence of the silicon pyramid morphology on the PL spectra of the perovskite thin film. (a) Scanning confocal microscopy map of PL peak energy at the height of maximum PL intensity, measured with a confocal laser scanning microscope with a $1/e^2$ spot size of 500 nm. (b) Scanning confocal light scattering image of the area measured in (a). (c) Simulated PL peak energy from a perovskite layer with thickness of 500 nm for emission from individual heights (relative to the pyramid peak height) at different pyramid heights. The border between the peak and valley regions as illustrated in (d) is given by the black dotted line. (d) Illustration of PL emission from valley and peak regions: PL emitted from the bottom of the structure is more redshifted due to stronger absorption end re-emission in the thicker perovskite region.

simulated in the ray-tracing model. In contrast to experiment, where even with localized excitation emission is still impacted by charge carrier diffusion, the model enabled the simulation of emission from singular heights. The results of this simulation are shown in Figure 3c, where the PL peak energies for emission from different heights and for different pyramid sizes are compared. The height from which the emission stems is defined relative to the height between the bottom (in the valley) and the top (at the tip) of the perovskite. To aid visual interpretation, valley and peak regions of the perovskite volume have been defined, as illustrated in Figure 3d. The border between these regions has been marked in the simulation results as well as in the illustration in Figure 3d with a dashed line. The findings from the simulation are consistent with the measurement: the signal emitted from the valley regions is redshifted relative to the peak regions. This is due to the large interaction volume for reabsorption and long mean optical path length between emission position and air-perovskite interface in the valleys. Similar to the effect occurring at larger perovskite thicknesses, this leads to a redshifted PL signal. In contrast, light in the peak regions has a significantly higher probability for escaping before reabsorption, resulting in a more blue-rich signal.

Comparing the simulated variation in the PL peak energy across the emission height range with the experimental data, a higher variation is observed in experiment: at an average pyramid size similar to the experiment of 3 μm the simulation shows a peak shift of the area-integrated PL spectrum of 29 meV, while the experiment shows 38.0 meV from valley to tip. This observation is similar to that found above for Figure 1 and is attributed to the effects mentioned in the corresponding section.

Both experiment and simulation in Figure 2 showed that for smaller pyramid sizes, a redshift of the global PL peak energy occurs relative to the case for larger pyramid sizes. This can now be related to the PL peak energy difference between emission from the valley and peak regions: For small pyramid sizes, the valley regions contain a large share of the overall perovskite volume. As a redshifted signal originates from this region, this larger volume share also results in a redshift of the global PL signal. With increasing pyramid size, the perovskite volume share of the valleys and therefore their impact on the global peak energy decreases, resulting in a reduction of this redshift. We note that this proposed explanation differs to the model by Lee et al. [25], that ascribes the redshifted emission from valley regions to increased mechanical strain or stress in the perovskite film. Our work shows quantitatively that a major fraction of the redshift is due to variation of light outcoupling across the pyramid structure. Thereby, we show the importance of the inhomogeneity of absorption and re-emission processes in the texture-dependent perovskite PL.

In addition, the spatially resolved emission behavior also provides a possible explanation of the redshift of the simulated global PL signal relative to experiment that was observed in the previous sections. In the model, homogeneous emission across the pyramid is assumed due to near-homogeneous absorption and sufficiently large diffusion length before recombination. Nevertheless, there is a decrease of the intensity absorbed low in the valley regions, as visible in Figure S5. If this is not completely compensated for by electron diffusion before recombination, this could favor emission from the peaks, resulting in a more blue-rich experimental result and therefore be responsible for the observed systematic shift. As with grain boundaries, this complex effect cannot be quantified exactly and does not have an impact on the relative trends discussed in this paper.

3 | Conclusion

The optical effects determining the PL spectrum for perovskite-coated silicon pyramid and flat substrates were investigated as a function of perovskite layer thickness and pyramid height. Photon reabsorption in the perovskite induces a redshift in the PL signal of which the magnitude is strongly dependent on the substrate geometry and perovskite thickness. We find that increasing the perovskite thickness on planar substrates induces a redshift of the PL spectrum at a rate of −27 meV/μm in the 450–1000 nm thickness range. For textured silicon substrates the perovskite PL spectrum redshifts by 47 meV/μm in the 300–650 nm thickness range. We established a statistical ray-optical simulation model that takes into account emission, absorption, and re-emission in the perovskite film for flat and textured geometries. The model shows a similar redshift of the PL signal with increasing perovskite thickness. In the thickness range of 300–1000 nm, the rate of this change in the simulation model is 15 meV/μm (planar) and −25 meV/μm, respectively. That rate of change in the simulation model is smaller than in experiment but shows that the reabsorption effect significantly contributes to the redshift observed in experiment.

Furthermore, we experimentally demonstrate that for a given perovskite thickness, pyramids with a small height show a larger redshift of the PL peak energy than pyramids with a large height. The contribution of reabsorption to this effect is again confirmed by the simulation model. By correlating local PL measurements with simulations, we reveal that this behavior is due to the increased contribution of valley regions where the reabsorption effect is more pronounced for smaller pyramids.

Our works show that the reabsorption effect can significantly influence the PL spectra measured for perovskite films with large thickness or deposited on textured substrates. It is essential to consider this effect when investigating bandgaps of materials and when optimizing two-terminal perovskite-silicon tandem solar cells. Based on this study, we, therefore, recommend that when comparing PL results between different perovskite thicknesses and substrate geometries or when determining the bandgap from PL measurements, complementary characterization techniques should be utilized to quantify the impact of reabsorption.

4 | Experimental Section

4.1 | Perovskite Fabrication

Prior to perovskite deposition, the substrates were cleaned. The cleaning procedure consisted of (1) blowing the substrates gently with N_2 to remove macroparticles, (2) dynamically spin coating a 200 μL volume of ethanol (EtOH) for 30 s to remove dust or other

particles, and (3) subjecting the substrates to a UV/ozone treatment for 15 min to eliminate contaminants from the surface. Following that, the hole transport layer (HTL) used in the usual tandem solar cell stack was deposited to maintain a similar perovskite growth as in a tandem device. The HTL consisted of [2-(9H-carbazol-9-yl)ethyl]phosphonic acid (2PACz) which was deposited via static spin coating (100 µL of a 7 mM solution of 2PACz in EtOH, 7 s waiting time, 3000 rpm for 30 s), followed by an annealing treatment at 100°C for 10 min. Both deposition and thermal treatments were carried out inside the glovebox (GB). Perovskite absorbers were deposited using the hybrid evaporation/spin coating method. In a first step, PbI_2 and CsI were thermally coevaporated in a Lesker Mini SPECTROS evaporator with a designated nominal thickness (mentioned in the main text). The evaporation rates were set to 1 Å/s (crucible temperature range: 285°C–320°C) and 0.1 Å/s (crucible temperature range: 390°C–430°C), respectively. The rates were controlled using quartz crystal sensors. The base pressure was $<2 \times 10^{-6}$ mbar while the working pressure was around 3×10^{-6} mbar. The substrate temperature was set to 20°C, and the rotation of the substrate to 20 rpm. In a second step, 150 µL of a FABr/FAI solution (in EtOH solvent) was dynamically spin coated at 2200 rpm onto the scaffold (in the GB) for 35 s, then annealed at 150°C for 20 mins in air (relative humidity ~35%–55%). The solution's organohalide ratio was set to FABr/FAI = 65/35 vol% and the concentration was optimized to achieve full or near-full conversion on the different substrates and for the different thicknesses (as shown in Section S1).

4.2 | X-Ray Diffraction (XRD)

XRD measurements were performed using a Bruker D8 Advance diffractometer (with a Cu anode at 40 mA/40 kV). The step size was set to 0.3° and the time per step to 0.1 s. The analysis software DIFRAC.EVA was used to assess the data.

4.3 | SEM

SEM measurements were carried out using a Schottky emission SEM from Zeiss with an Auriga 60 model. Top-view and cross-sectional images were captured using an In-lens detector with an acceleration voltage of 5 kV. In the top-view mode, an angle of 45° was set to take the images.

4.4 | X-Ray Photoelectron Spectroscopy (XPS)

XPS measurements were conducted in a Thermo Fisher Scientific Nexsa G2 photoelectron spectrometer with monochromatized Al Kα emission at 1486.6 eV as excitation source. Survey spectra were recorded with a pass energy of 200 eV. Depth profiling was achieved by erosion with Ar^+ ions at 1 keV kinetic energy with the ion gun operating in 'low current' mode over an area of $2 \times 2\ mm^2$, yielding a rate of ~0.09 nm/s on Ta_2O_5. Zalar rotation with ~10 rpm was used for more conformal removal of material. The data were quantified with the Avantage software utilizing instrument-specific relative sensitivity factors (RSF).

4.5 | Steady-State Spectrally Resolved PL

PL measurements were carried out using a LUQY Pro instrument from Quantum Yield Berlin (QYB). The measurements were performed under a 532 nm-laser illumination with a spot size of 0.1 cm^2 and a measurement time of 3 s. To mimic the real-world operation scenario, the laser power density was set to equal to that of the AM1.5G solar spectrum (1000 W/m^2) (automatically calculated for the selected spot size as well as short-circuit current density (j_{SC}) and (EQE) at 532 nm). Emitted light is collected across the entire hemisphere using an integrating sphere.

4.6 | Spatially Resolved Confocal PL

The spatially resolved confocal PL maps were taken using a WITec alpha300 RS confocal microscopy setup in reflection mode, with a 100x objective and a numerical aperture of 0.9. The textured samples were excited with 405 nm continuous-wave laser light with 5 µW power, and a $1/e^2$ diameter spot size of approximately 500 nm. Spectra were collected with a fiber-connected WITec UHTS spectrometer, where a photonic crystal acts as a confocal pinhole. The $40 \times 40\ \mu m^2$ PL maps were taken by moving the sample with a piezo-electric stage, adjusting the height of the focal plane by 1 µm between each successive map. As illumination with a high power density could induce halide segregation in the perovskite, which in turn redshifts the PL, the laser power of 5 µW was chosen and optimized to balance halide segregation and the signal-to-noise ratio. To quantify this effect for the above laser power, two consecutive PL maps were taken on the same area, which doubled the total absorbed power. The result of these measurement is shown in Section S6, indicating that the effects of halide segregation are minor compared to the effect of reabsorption. To further ensure that the measured redshift in the valleys is not solely induced by halide segregation, stacks have always been measured from valleys to peaks, such that redshifts induced by re-exposing the perovskite are minimized for the valley regions. Finally, prior to each map acquisition, one light soaking map with the same laser power was taken, to bring the perovskite in a stable regime. For the final PL peak position map (Figure 3a), only the highest intensity values at each pixel position, across all focus planes, were used to ensure optimal in-focus representation. Finally, spline interpolation is applied to the dataset to improve the visualization of the red and blue-shifted regions,

4.7 | Raytracing Model

Optical modeling is conducted using the raytracing software Raytrace3D [29, 30], which was previously used to successfully describe experimental reflection data of structured silicon in combination with a thin film system in [31]. The simulation model uses regular upright pyramids with a pyramid angle of 48° (compare Section S4), which show similar behavior to random pyramids in the wavelength range considered [32]. Regular pyramids have been chosen to allow for the isolated evaluation of the impact of pyramid size. The optical behavior of the perovskite–silicon interface, including the HTL, is calculated using the transfer matrix formalism [33]. Perfect conformal coating of the perovskite layer onto silicon is assumed. Light propagation within the perovskite layer is treated as incoherent, as due

to the varying thickness and grain boundaries, it cannot be considered as a perfectly planar layer of constant thickness [34]. For internal emission, each simulation traces 5 million rays, emitted isotropically from 0.5 million sources which are each placed at a randomized location in the defined emission volume. Each ray is traced until it reaches the detector, or its intensity is reduced by a factor of one million through absorption. For the spectral intensity distribution, the generalized Kirchhoff law [35] is employed. Section S5 gives justification of homogeneous emission distribution. Emission after reabsorption is assumed to result in the same spectral distribution as the initial emission and is therefore not considered separately, as no absolute intensities are evaluated. For the refractive index data, the same datasets as in ref. [34] were used, with the 2PACz assumed to have a thickness of 1 nm and similar optical properties as PTAA. For the perovskite, a new dataset has been calculated as described in the following section. The same layer stack as in experiment was simulated. Rays leaving the silicon-perovskite structure are detected under the full 2π steradian upper hemisphere. The simulation was conducted with a wavelength step of 1 nm, with peak position extracted using cubic spline interpolation after noise reduction using the method of Savitzky and Golay [36].

4.8 | Determination of k-Data within the Urbach-Tail

The refractive index data of the perovskite in use were determined using angle-resolved spectroscopic ellipsometry (M-2000F, J. A. Woollam Co., Inc.), using 407 nm thick planar perovskite layer on a planar silicon substrate, deposited as described above. Close to the Urbach-Tail, there is only very weak absorption. Therefore, the refractive index data in this region were extracted from a PL measurement. For this, single-pass Lambert–Beer absorption was assumed as well as homogeneous emission from the perovskite layer. Only light initially emitted within the emission cone is considered. The second-order effects of path length increase within the emission cone, reflection at the silicon backside, and reflection at the perovskite-air interface are omitted, especially because of the latter two are expected to approximately cancel each other out. Internal refraction is also assumed to have a minor effect. Following these assumptions, the external emission $E(\hbar\omega)$ is expected to be

$$E(\hbar\omega) = E_0(\hbar\omega) \cdot \frac{[1 - \exp(-\alpha(\hbar\omega) \cdot t)]}{\alpha(\hbar\omega) \cdot t}$$

with t the absorber layer thickness and $E_0(\hbar\omega)$ the internally emitted signal as derived from the generalized Kirchhoff law [35]. From the reference PL measurements, only the relative shape of the external emission is known $E(\hbar\omega) = F \cdot PL(\hbar\omega)$ with F as a fitting factor. This factor has been fitted to obtain a good match with the ellipsometry data. From this, the absorption coefficient for the Urbach tail region could be extracted and combined with the ellipsometry data to obtain the dataset used within this work, which is displayed in Figure S8.

Acknowledgments

This work was funded by the Fraunhofer Gesellschaft within the ICON project MEEt and the LIGHTHOUSE PROJECT MaNiTU, as well as by the German Federal Ministry for Economic Affairs and Climate Action within the project PrEsto (No. 03EE1086A). This work is further supported by ERC grant PHASE (No. 101125948) and by the Vector Stiftung's funding of J. Borchert's independent research group. A. Callies gratefully acknowledges scholarship support (20021/728−242) from the Deutsche Bundesstiftung Umwelt (DBU). Work at AMOLF is part of the research program of SolarLab within SolarNL, a national research, innovation and industrial development program funded by the Netherlands National Growth Fund. We thank J. Zielonka for her support with SEM measurements, F. Martin for the support with reflection measurements, M. Hanser for the support with ellipsometry measurements, M. Bivour, K. Zimmermann and H. Nagel with silicon bottom solar cell processing, P. Schöttl for support with the raytracing software, Singulus for providing silicon substrates with different textures as part of project PrEsto, K. Fischer and J. Myers for technical support, O. Fischer and P. Schygulla for fruitful discussions.

Conflicts of Interest

The authors declare no conflicts of interest.

Data Availability Statement

The data that support the findings of this study are available from the corresponding author upon reasonable request.

References

1. A. Callies, M. Hanser, J. C. Goldschmidt, B. Bläsi, and O. Höhn, *Optics Express* 31 (2023): 19428–19442.

2. F. Gota, R. Schmager, A. Farag, and U. W. Paetzold,*Optics Express* 30 (2022): 14172–14188.

3. J. Lehr, M. Langenhorst, R. Schmager, et al., *Sustainable Energy & Fuels* 2 (2018): 2754–2761.

4. N. Tucher, O. Höhn, J. N. Murthy, et al., *Optics Express* 27 (2019): A1419–A1430.

5. F. Sahli, J. Werner, B. A. Kamino, et al., *Nature Materials* 17 (2018): 820–826.

6. Z. Liu, Z. Xiong, S. Yang, et al., *Joule* 8 (2024): 2834–2850.

7. O. Er-raji, M. A. Mahmoud, O. Fischer, et al., *Joule* 8 (2024): 2811–2833.

8. X. Y. Chin, D. Turkay, J. A. Steele, et al., *Science* 381 (2023): 59–63.

9. H. Luo, X. Zheng, W. Kong, et al., *ACS Energy Letters* 8 (2023): 4993–5002.

10. X. Luo, H. Luo, H. Li, et al., *Advanced Materials* 35 (2023): e2207883.

11. X. Zheng, W. Kong, J. Wen, et al., *Nature Communications* 15 (2024): 4907.

12. R. Patidar, D. Burkitt, K. Hooper, D. Richards, and T. Watson, *Materials Today Communications* 22 (2020): 100808.

13. O. Kunz, J. W. Weber, G. Rey, M. Juhl, and T. Trupke, *Solar RRL* 8 (2024): 2400385.

14. T. Kirchartz, J. A. Márquez, M. Stolterfoht, and T. Unold, *Advanced Energy Materials* 10(2020): 1904134.

15. L. E. Mundt, F. D. Heinz, S. Albrecht, et al., *IEEE Journal of Photovoltaics* 7 (2017): 1081–1086.

16. O. Fischer, A. D. Bui, F. Schindler, et al., *Progress in Photovoltaics: Research and Applications* 33 (2023): 3754.

17. M. Demant, S. Rein, J. Haunschild, et al., *Progress in Photovoltaics: Research and Applications* 24 (2016): 1533–1546.

18. A. Al-Ashouri, E. Köhnen, B. Li, et al., *Science* 370 (2020): 1300–1309.

19. T. W. Crothers, R. L. Milot, J. B. Patel, et al., *Nano Letters* 17 (2017): 5782–5789.

20. P. Fassl, V. Lami, F. J. Berger, et al., *Matter* 4 (2021): 1391–1412.

21. J. B. Patel, A. D. Wright, K. B. Lohmann, et al., *Advanced Energy Materials* 10 (2020): 1903653.

22. J. A. Giesecke, M. Kasemann, M. C. Schubert, P. Würfel, and W. Warta, *Progress in Photovoltaics: Research and Applications* 18 (2010): 10–19.

23. M. de Bastiani, R. Jalmood, J. Liu, et al., *Advanced Functional Materials* 33 (2023): 2205557.

24. E. M. Tennyson, K. Frohna, W. K. Drake, et al., *ACS Energy Letters* 6 (2021): 2293–2304.

25. S.-W. Lee, S. Bae, J.-K. Hwang, et al., *Communications Chemistry* 3 (2020): 37.

26. O. Er-raji, L. Rustam, B. P. Kore, S. W. Glunz, and P. S. C. Schulze, *ACS Applied Energy Materials* 6 (2023): 6183–6193.

27. O. Er-raji, C. Messmer, A. J. Bett, et al., *Solar RRL* 7 (2023): 2300659.

28. O. Er-raji, A. J. Bett, S. Lange, et al., *Progress in Photovoltaics: Research and Applications* 33 (2025): 86–99.

29. R. Banke and A. Heimsath, "*Raytrace3D-Power Tower - A Novel Optical Model For Central Receiver Systems*," 16th SolarPACES Conference, Perpignan, France, September 2010.

30. P. Schöttl, G. Bern, P. Nitz, F. Torres, and L. Graf, "*RAYTRACE3D by Fraunhofer ISE. Accurate and Efficient Ray Tracing for Concentrator Optics*," accessed March 24, 2025, https://www.ise.fraunhofer.de/content/dam/ise/de/downloads/pdf/raytrace3d.pdf.

31. N. Tucher, J. Eisenlohr, P. Kiefel, et al., *Optics Express* 23 (2015): A1720–A1734.

32. S. C. Baker-Finch and K. R. McIntosh, *Progress in Photovoltaics: Research and Applications* 19 (2011): 406–416.

33. H. A. Macleod, *Thin-Film Optical Filters*, 4th ed. (CRC Press, 2010).

34. C. Messmer, B. S. Goraya, S. Nold, et al., *Progress in Photovoltaics: Research and Applications* 29 (2021): 744–759.

35. P. Würfel, *Journal of Physics C: Solid State Physics* 15 (1982): 3967–3985.

36. A. Savitzky and M. J. E. Golay, *Analytical Chemistry* 36 (1964): 1627–1639.

Supporting Information

Additional supporting information can be found online in the Supporting Information section.